

3D Magnetic Resonance Microscopy of the Ex Vivo Retina

Bryan H. De La Garza,¹ Eric R. Muir,¹ Yen-Yu I. Shih,¹ and Timothy Q. Duong^{1–5*}

3D-MR microscopy at 11.7T and $20 \times 20 \times 57 \mu\text{m}$ resolution was performed on formalin-fixed rat eyes with: (I) no contrast agent and (II) Gadodiamide (Omniscan[®]) added to the fixative. Group I data showed generally poor contrast among layers. Group II data showed markedly better lamina-specific contrast with the nerve fiber + ganglion cell layer and inner nuclear layer being hypointense, and the inner plexiform, outer plexiform, outer nuclear layer, and the segments being hyperintense. The signal-to-noise ratio in group II was higher than group I, consistent with Gadodiamide acting as a T_1 -contrast agent. All major retinal layers were assigned and their thicknesses quantified with corroboration by histology. MR microscopy allows nondestructive examination of valuable specimens and could have applications in disease and in vivo. Magn Reson Med 000:000–000, 2011. © 2011 Wiley-Liss, Inc.

Key words: ultra high-resolution MRI; high field; MRI contrast agents; T_1 and T_2 contrast; manganese; MEMRI; photo-receptors

INTRODUCTION

The retina consists of multiple distinct stratified layers (1). From the vitreo-retinal interface, the major layers are the nerve fiber layer (NFL) + ganglion cell layer (GCL), inner plexiform layer (IPL), inner nuclear layer (INL), outer plexiform layer (OPL), outer nuclear layer (ONL), inner segment (IS), and outer segment (OS). The interspersed plexiform layers are synaptic links between the adjacent nuclear layers. The choroid vascular layer is located external to the neural retina, behind the OSs and the retinal pigment epithelium.

Magnetic resonance imaging (MRI) has been used to image anatomical layers in the mouse (2), rat (3), and cat (4) retinas; relaxation and diffusion time constants of different layers in the cat (4), rat (5), and mouse retinas (6); blood-oxygenation level dependent (BOLD) responses to physiological (3) and visual (7–9) stimulations of the rat

and cat retinas; and quantitative blood flow by continuous arterial spin labeling (10,11). MRI has also been applied to study retinal degeneration (3,10), diabetic retinopathy (12), and glaucoma (13) in rodents. Typically, 1–4 MRI layers were visible. Blood-oxygenation level dependent (14) and blood-flow (15,16) MRI of the human retina have also been reported.

With magnetic resonance microscopy (MRM), anatomical imaging of ex vivo samples (17,18) can achieve typical resolutions of $50 \mu\text{m} \times 50 \mu\text{m} \times 50 \mu\text{m}$ to $7.8 \mu\text{m} \times 7.8 \mu\text{m} \times 7.8 \mu\text{m}$ (19). The nondestructive nature of MRM allows repeated studies of valuable specimens, perfectly registered images obtained with different contrasts, and virtual sectioning at any plane from the 3D data sets free of labor-intensive histological sample processing and tissue distortion. Contrast agents, such as Gadodiamide (Omniscan), have been utilized to enhance signal-to-noise ratio (SNR) and contrast-to-noise ratio in ex vivo brain diffusion-tensor imaging studies (20).

The goal of this study was to explore the use of high-resolution 3D MRM to image multiple retinal layers of the rat eye ex vivo at $20 \times 20 \times 57 \mu\text{m}$. To augment SNR, a custom-made radiofrequency transmitter-receiver and high magnetic field (11.7 Tesla) scanner were used. To augment SNR and contrast-to-noise ratio, the Gadodiamide MRI contrast agent was utilized. MRM was performed on ex vivo fixed eyes with and without contrast agent. Comparisons were made with histology of closely matched sections.

MATERIALS AND METHODS

Sample Preparations

Animal experiments were performed with IACUC approval and in accordance with the ARVO Statement for the Use of Animals in Ophthalmic and Vision Research. Experiments were performed on two groups of normal adult Sprague Dawley rats (250–350 g). In Group I ($n = 2$), eyes of the euthanized rats were enucleated and fixed with 10% neutral buffered formalin. In Group II ($n = 5$), eyes of the euthanized rats were enucleated and promptly injected with 10 μL of a 20:1 solution of neutral buffered formalin (10%) to Gadodiamide (0.5 M Omniscan[®]) into the vitreous via a 30-gauge needle and a Hamilton syringe, immersed in 20:1 formalin: Gadodiamide solution for 6 h, and then transferred to a 160:1 formalin:Gadodiamide solution (21). The enucleated eyes were stored in the 160:1 formalin:Gadodiamide solution for 2 days to ensure adequate fixation. The eyes were immobilized in a custom-made plastic holder filled with 10% formalin for imaging.

¹Research Imaging Institute, University of Texas Health Science Center, San Antonio, Texas.

²Department of Ophthalmology, University of Texas Health Science Center, San Antonio, Texas.

³Department of Radiology, University of Texas Health Science Center, San Antonio, Texas.

⁴Department of Physiology, University of Texas Health Science Center, San Antonio, Texas.

⁵Research Division, South Texas Veterans Health Care System, San Antonio, Texas.

Grant sponsor: NIH/NEI; Grant numbers: R01 EY014211, EY018855, and R01EY09702; Grant sponsor: MERIT Award from the Department of Veterans Affairs.

*Correspondence to: Timothy Q. Duong, Ph.D., Research Imaging Institute, University of Texas Health Science Center at San Antonio, 8403 Floyd Curl Dr, San Antonio, TX 78229. E-mail: duongt@uthscsa.edu

Received 16 March 2011; revised 17 May 2011; accepted 14 June 2011.

DOI 10.1002/mrm.23082

Published online in Wiley Online Library (wileyonlinelibrary.com).

MRM

MRM experiments were performed on a Bruker 11.7-Tesla/16-cm scanner (Billerica, MA). A custom-built, small single-loop surface coil (inner diameter = 1cm) encircled the sample holder. 3D FLASH MRI was acquired using TR = 39 ms, TE = 7.46 ms, data matrix = $360 \times 360 \times 128$, and FOV = $7.3 \text{ mm} \times 7.3 \text{ mm} \times 7.3 \text{ mm}$, yielding an in-plane resolution of $20 \times 20 \times 57 \mu\text{m}$. Repetitions were acquired in 30-min blocks. A total of 42 blocks were acquired. The 3D data set was zero-filled by a factor of two in the frequency and the first phase-encode directions, and a factor of 4 in the second phase encode direction, yielding a nominal resolution of $10 \times 10 \times 14 \mu\text{m}$.

Image Data Analysis

All data analysis used programs written in Matlab (Math-Works, Natick, MA) and 3D data were visualized using MANGO (<http://ric.uthscsa.edu/mango/download.html>). The time series data were co-registered as needed before averaging. To quantitatively determine laminar thickness, the retina was automatically detected using an edge-detection technique as previously described (3). Radial projections perpendicular to the vitreous boundary were obtained with three or four times the sampling density of the original image. The projection profiles were averaged along a small portion of the retina, within $\pm 0.5 \text{ mm}$ from the optic nerve head as shown in Fig. 3 inset. Thicknesses of alternating dark and bright layers were determined using the “half height” method. MRI and histological thicknesses were correlated for individual layer thicknesses and total thicknesses. To evaluate the effects of image slice thickness on laminar resolution, different image thicknesses were reconstructed from the 3D data set.

Histology

After MRM, the eyes were processed. Samples were washed with a graded series of alcohols, embedded in paraffin, and sectioned at $10 \mu\text{m}$. Standard hematoxylin and eosin (H&E) staining was performed. Each histological section was photographed and laminar thicknesses were measured. Histology slides were carefully matched with MRM images for comparison. Laminar thicknesses were measured with an Olympus BX60 microscope under $100\times$ magnification.

RESULTS

Figure 1 shows a representative single slice bisecting the optic nerve head from a 3D data set of group I (no contrast agent). Although the spatial resolution was adequate and some contrast was evident in the retina, the contrast was inadequate to differentiate major retinal layers unambiguously. Layer assignments were thus not made.

Figure 2 shows a single slice bisecting the optic nerve head and the corresponding histology slide from an animal in group II. SNR and contrast-to-noise ratio of group II were higher than those of group I. The indentation of

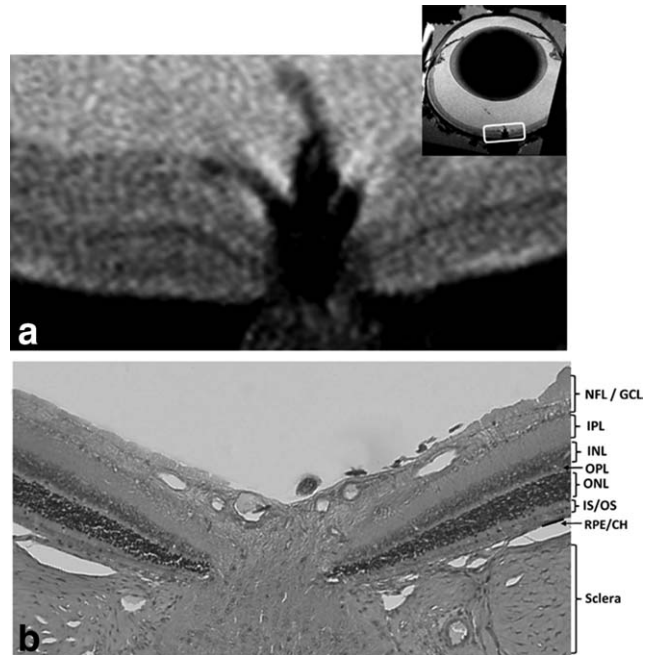


FIG. 1. **a:** A single MRM slice bisecting the optic nerve head from group I (no contrast agent) at $10 \times 10 \times 14 \mu\text{m}$ nominal resolution and $20 \times 20 \times 57 \mu\text{m}$ actual resolution taken from a 3D data set. The inset shows the location of the expanded view. **b:** The corresponding closely matched histological slide from the same rat eye. Although the spatial resolution was high, contrast was poor.

the optic cup around the optic nerve head, the hyaloid canal, and the characteristic convergence of various retinal layers around the optic nerve head were evident. Excellent spatial resolution and contrast among different retinal layers were observed. The hypointense layers were assigned to be NFL/GCL and INL, which contain the nuclear cell bodies. The interleaving hyperintense layers were assigned to be the IPL and OPL, ONL, and the IS/OS. The ONL also had a thin hypointense layer at its inner edge.

Automated profile analysis allowed objective and robust determination of layer thicknesses for group II. Figure 3 shows the profile analysis along with the matching MRM and histological sections. The flattened MRM retinal image and the corresponding histology showed excellent correspondence.

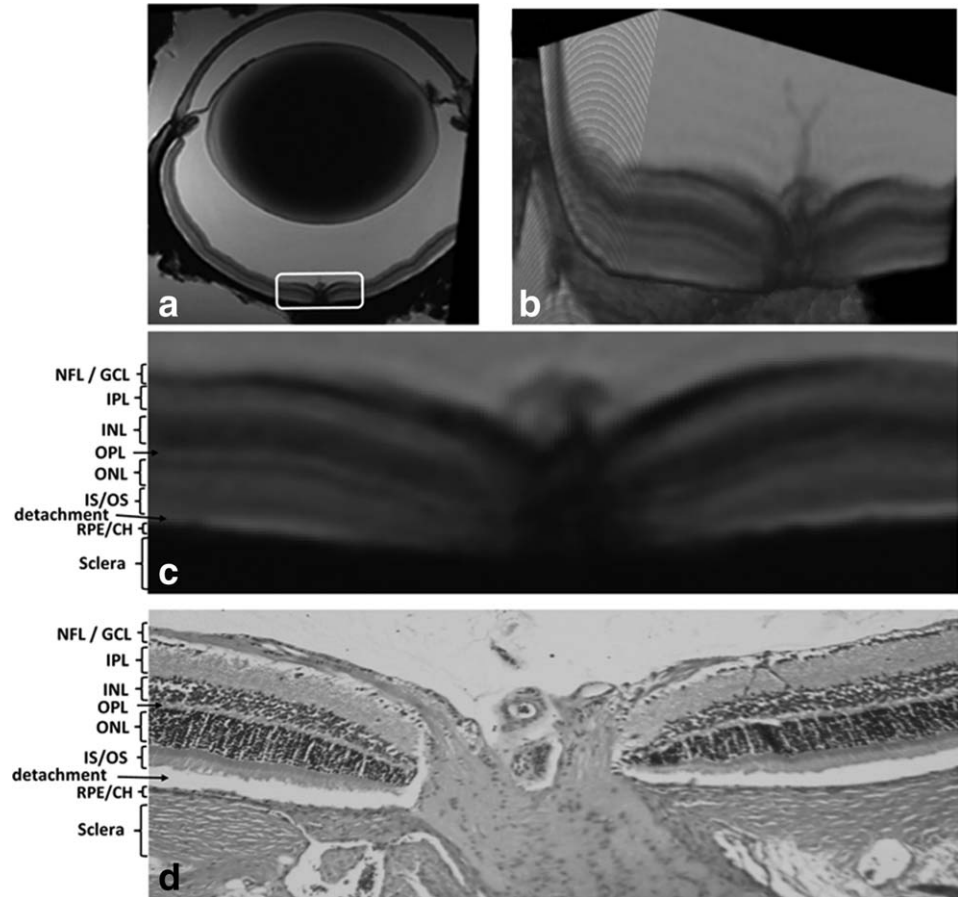
Figure 4 shows the scatter plot of MRI and histological thickness of different retinal layers from individual animals and the bar graph of the group-averaged data. Layer thicknesses by MRI agree with those by histology, albeit there were statistical differences between MRI and histological thicknesses for some layers. The total thicknesses of the neural retina were $241 \pm 13 \mu\text{m}$ by MRI and $228 \pm 11 \mu\text{m}$ by histology (mean \pm SD, $N = 5$).

Figure 5 illustrate the effects of image slice thickness on layer resolution. With increasing thicknesses, the layer assignments became less distinguishable.

DISCUSSION

High-resolution and high-contrast MRM was developed and applied to image multiple layers in the rat retina

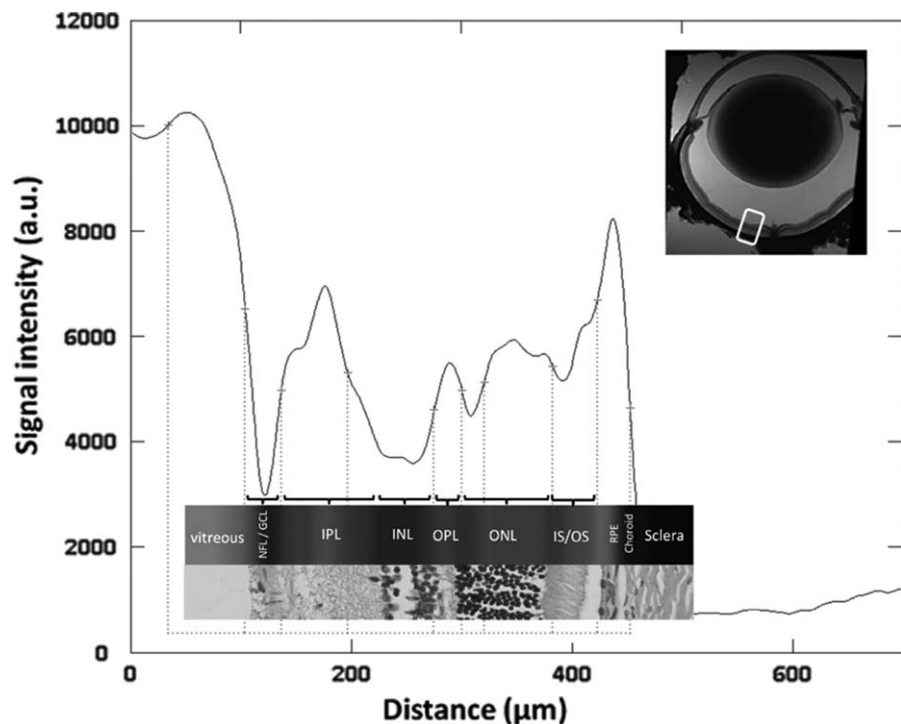
FIG. 2. **a**: A single MRM slice bisecting the optic nerve head taken from a 3D data set at $10 \times 10 \times 14 \mu\text{m}$ nominal resolution and $20 \times 20 \times 57 \mu\text{m}$ actual resolution from group II (Gadodiamide soaked), **b**: a cut-away 3D view of the 3D data, **c**: an expanded view of the single slice taken from the MRM 3D data set, and **d**: the corresponding closely matched histological slide from the same rat eye. The indentation around the optic nerve, the hyaloid canal, and the characteristic convergence of various retinal layers around the optic nerve head are evident. Layer assignments are shown on the figure. NFL, nerve fiber layer; GCL, ganglion cell layer; IPL, inner plexiform layer; INL, inner nuclear layer; OPL, outer plexiform layer; ONL, outer nuclear layer; IS/OS, inner/outer photoreceptor segment layer; RPE, retinal pigment epithelium; CH, choroidal vascular layer.



ex vivo, approximating histological resolution and contrast. Gadodiamide improves SNR and contrast-to-noise ratio, and differentially enhances various layers within

the retina. By matching with histological slides, all major retinal layers were unambiguously assigned and their thicknesses quantified. To our knowledge, this is the

FIG. 3. Intensity profile obtained using automated profile analysis with matching linearized MRM and histological sections of the retina from a rat in group II. The inset shows a single slice taken from a 3D data set and the white rectangle shows the area that this profile was analyzed. Black brackets show the layer assignments based on the peaks and valleys of signal intensity plot. The flattened MRM retinal image and the corresponding histology are shown for comparison.



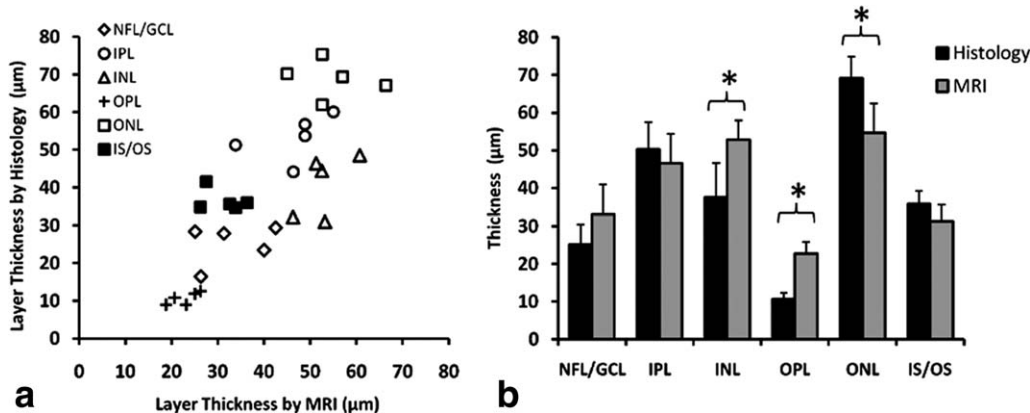


FIG. 4. **a**: Scatter plot of MRI and histological thickness of different retinal layers from individual animals. Each data point came from one animal. MRI and histological layer thickness correlation yielded a R^2 of 0.55. **b**: group-averaged MRI and histological thickness of different retinal layers (mean \pm SD, $N = 5$, * $P < 0.05$).

first 3D MRM study of the retina that demonstrates histologically defined, multi-layer structures of the retina at very high spatial resolution and contrast. This study sets the stage for applications in retinal diseases *ex vivo* as well as exploring similar high-resolution MRM in the *in vivo* retina.

Contrast Mechanisms and Layer Assignments

By comparison with group I data, group II showed that the Gadodiamide improved contrast among different laminar structures. This contrast agent enhanced innate tissue properties, including contrast water density and/or water mobility among different retinal layers. Although fixed postmortem tissue likely results in loss of some extracellular compartmentation of the contrast agents, some compartmentation is sufficient to yield differential signals among different layers.

In group II, the GCL and INL were mostly hypointense whereas the interleaving plexiform layers (IPL and OPL), ONL and the IS/OS were hyperintense. Gadodiamide in this preparation was likely preferentially localized to the extracellular space because the cell membrane likely presents as a partial barrier postmortem. The SNR of group II was better than group I, suggesting that Gadodiamide acted as a T_1 contrast agent. The alternate explanation that Gadodiamide attenuated signals by T_2^* mechanism in the NFL/GCL and INL was unlikely because the other layers (IPL, OPL, ONL, IS/OS) had better SNR than those of group I. We thus concluded that the contrast mechanism in the retina soaked with Gadodiamide was dominated by T_1 -weighting under these experimental conditions.

Layer Assignments and Thicknesses

The data presented here demonstrated improved resolution and contrast sufficient to visualize additional and histologically defined laminar structures that were not detectable previously by MRI. Thickness analysis was performed (for group II). Layer assignments are in excellent agreement with those by optical coherence tomography in rodent retina (22–24). In the MRM data, the dark

band between OPL and ONL appeared to be the interface between OPL and ONL, consistent with those assigned using optical coherence tomography (22–24).

The total thickness of the *ex vivo* neural retina in our study was 241 ± 13 μm by MRI and 228 ± 11 μm by histology (mean \pm SD, $N = 5$). The slight shrinkage is expected due to the additional preparation steps in the histological preparation. Thickness of the rat neural retina has been reported to be 187 μm by *in vivo* MRI and 169 μm by histology (3), and thickness of the mouse neural retina has been reported to be 182 ± 7 μm by *in vivo* MRI, 159 ± 10 μm paraffin embedding, and 220 ± 17 μm by frozen cut (6). The total normal mouse neural retina thickness by optical coherence tomography has been reported to be 220–250 μm (24) and 237 ± 2 μm (22). We did not analyze the choroid thickness as it usually detached to a larger extent in the sectioned histological slides, making it difficult to compare with MRM data of the intact eye. Comparisons of the *ex vivo* retina

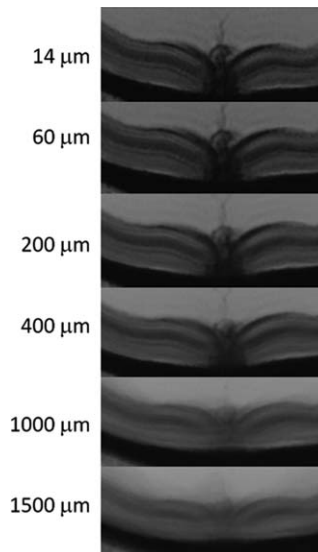


FIG. 5. The effects of image slice thickness on laminar resolution. MRI images at different slice thickness were obtained by summing up neighboring slices from the 3D data set.

across different laboratories need to be made with caution due to potentially different experimental conditions. Retinal layer thicknesses were also dependent on the fixative, its concentration, and fixation duration (data not shown).

Retinal layers became less distinguishable with increasing reconstructed image slice thicknesses. Under these experimental conditions, contrasts among different layers were clearly distinguishable up to 400 μm . The total retinal thickness was however not significantly affected at least up to 1.5-mm image slice thickness in the rat retina. These findings have implications in MRI of the in vivo retina which may be limited by shorter scan time and physiological noises.

CONCLUSIONS

This study reported high-resolution 3D anatomical MRM of the ex vivo retina at $20 \times 20 \times 57 \mu\text{m}$, providing remarkable contrast among different layers in the rat retina. All major retinal layers were assigned and their thicknesses quantified with histological correlation. 3D MRM of the retina allows repeated nondestructive studies of the same sample, does not require labor intensive sectioning, avoids tissue distortion from sectioning, avoids misalignment of sectioned slides, and allows virtual sectioning at any plane from the 3D data sets. Future 3D MRM studies will explore imaging molecular contrast agents targeted to specific cell layers, light-versus-dark adaptation, disease-induced changes ex vivo, and in vivo application at similarly high spatial resolution.

REFERENCES

- Wassle H, Boycott BB. Functional architecture of the mammalian retina. *Physiol Rev* 1991;1:447–480.
- Muir ER, Duong TQ. Layer-specific functional and anatomical MRI of the retina with passband balanced SSFP. *Magn Reson Med* 2011, in press.
- Cheng H, Nair G, Walker TA, Kim MK, Pardue MT, Thule PM, Olson DE, Duong TQ. Structural and functional MRI reveals multiple retinal layers. *Proc Natl Acad Sci U S A* 2006;103:17525–17530.
- Shen Q, Cheng H, Pardue MT, Chang TF, Nair G, Vo VT, Shonat RD, Duong TQ. Magnetic resonance imaging of tissue and vascular layers in the cat retina. *J Magn Reson Imaging* 2006;23:465–472.
- Nair G, Shen Q, Duong TQ. Relaxation time constants and apparent diffusion coefficients of rat retina at 7 Tesla. *Int J Imaging Syst Technol* 2010;20:126–130.
- Chen J, Wang Q, Zhang H, Yang X, Wang J, Berkowitz BA, Wickline SA, Song SK. In vivo quantification of $T(1)$, $T(2)$, and apparent diffusion coefficient in the mouse retina at 11.74T. *Magn Reson Med* 2008;59:731–738.
- Duong TQ, Ngan S-C, Ugurbil K, Kim S-G. Functional magnetic resonance imaging of the retina. *Invest Ophthalmol Vis Sci* 2002;43:1176–1181.
- De La Garza B, Li G, Muir E, Shih YY, Duong TQ. BOLD fMRI of visual stimulation in the rat retina at 11.7 Tesla. *NMR Biomed* 2011;24:188–193.
- Shih YY, De La Garza BH, Muir ER, Rogers WE, Harrison JM, Kiel JW, Duong TQ. Lamina-specific functional MRI of retinal and choroidal responses to visual stimuli. *Invest Ophthalmol Vis Sci* 2011, in press.
- Li Y, Cheng H, Shen Q, Kim M, Thule PM, Olson DE, Pardue MT, Duong TQ. Blood-flow magnetic resonance imaging of retinal degeneration. *Invest Ophthalmol Vis Sci* 2009;50:1824–1830.
- Muir ER, Duong TQ. MRI of retinal and choroid blood flow with laminar resolution. *NMR Biomed* 2011;24:216–223.
- Berkowitz BA, Kowluru RA, Frank RN, Kern TS, Hohman TC, Prakash M. Subnormal retinal oxygenation response precedes diabetic-like retinopathy. *Invest Ophthalmol Vis Sci* 1999;40:2100–2105.
- Calkins DJ, Horner PJ, Roberts R, Gradianu M, Berkowitz BA. Manganese-enhanced MRI of the DBA/2J mouse model of hereditary glaucoma. *Invest Ophthalmol Vis Sci* 2008;49:5083–5088.
- Zhang Y, Peng Q, Kiel JW, Rosende CA, Duong TQ. Magnetic resonance imaging of vascular oxygenation changes during hyperoxia and carbogen challenges in the human retina. *Invest Ophthalmol Vis Sci* 2011;52:286–291.
- Peng Q, Zhang Y, Oscar San Emeterio Nateras O, van Osch MJP, Duong TQ. Magnetic resonance imaging of blood flow of the human retina. *Magn Reson Med* 2011;65:1768–1775.
- Maleki N, Dai W, Alsop DC. Blood flow quantification of the human retina with MRI. *NMR Biomed* 2011;24:104–111.
- Badea A, Johnson GA, Williams RW. Genetic dissection of the mouse brain using high-field magnetic resonance microscopy. *Neuroimage* 2009;45:1067–1079.
- Petiet AE, Kaufman MH, Goddeeris MM, Brandenburg J, Elmore SA, Johnson GA. High-resolution magnetic resonance histology of the embryonic and neonatal mouse: a 4D atlas and morphologic database. *Proc Natl Acad Sci U S A* 2008;105:12331–12336.
- Flint JJ, Lee CH, Hansen B, Fey M, Schmidig D, Bui JD, King MA, Vestergaard-Poulsen P, Blackband SJ. Magnetic resonance microscopy of mammalian neurons. *Neuroimage* 2009;46:1037–1040.
- D'Arceuil HE, Westmoreland S, de Crespigny AJ. An approach to high resolution diffusion tensor imaging in fixed primate brain. *Neuroimage* 2007;35:553–565.
- Petiet A, Hedlund L, Johnson GA. Staining methods for magnetic resonance microscopy of the rat fetus. *J Magn Reson Imaging* 2007;25:1192–1198.
- Huber G, Beck SC, Grimm C, Sahaboglu-Tekgoz A, Paquet-Durand F, Wenzel A, Humphries P, Redmond TM, Seeliger MW, Fischer MD. Spectral domain optical coherence tomography in mouse models of retinal degeneration. *Invest Ophthalmol Vis Sci* 2009;50:5888–5895.
- Ruggeri M, Wehbe H, Jiao S, Gregori G, Jockovich ME, Hackam A, Duan Y, Puliafito CA. In vivo three-dimensional high-resolution imaging of rodent retina with spectral-domain optical coherence tomography. *Invest Ophthalmol Vis Sci* 2007;48:1808–1814.
- Li Q, Timmers AM, Hunter K, Gonzales-Pola C, Lewin AS, Reitze DH, Hauswirth WW. Noninvasive imaging by optical coherence tomography to monitor retinal degeneration in the mouse. *Invest Ophthalmol Vis Sci* 2001;42:2981–2989.